RESEARCH ARTICLE

NANO · MICRO small
www.small-journal.com

3D-Printed $KVPO_4F$/rGO Aerogel Electrodes as High-Performance 5V-Class Cathode for Advanced Potassium-Ion Battery

Jinwei Zhang, Xiaolin Zhang, Junmin Xu, Xinyue Li, Dezhi Xiao, Zhixia Duan, Han Zhou, Xinchang Wang,* and Paul K. Chu**

A porous $KVPO_4F$/reduced graphene oxide (KVPF/rGO) microgrid aerogel electrode is designed and fabricated using direct ink writing 3D printing for high-performance potassium-ion battery cathodes. This 3D-printed KVPF/rGO aerogel electrode, which integrates well-dispersed $KVPO_4F$ microspheres in the reduced graphene oxide matrix, shows enhanced structural integrity and electrical conductivity, thereby facilitating efficient ion and electron transport. The KVPF/rGO electrode achieves a reversible discharge capacity of 99.0 mAh g^{-1} at a current density of 50 mA g^{-1} in the voltage range between 2.0 and 5.0 V. It retains 93.9% of its capacity after 100 cycles and delivers a discharge capacity of 72.6 mAh g^{-1} at a high current density of 500 mA g^{-1}, demonstrating good rate capability. The role of rGO in improving charge transfer and minimizing polarization is demonstrated. The flexibility of the 3D-printed electrodes is validated by fabricating soft-pack batteries, which maintain stable performance under mechanical stress, an essential requirement for wearable electronics. The results highlight the large potential of 3D printing technology to enhance the properties and flexibility of potassium-ion batteries and pave the way for future advancements in energy storage devices.

1. Introduction

With the increasing adoption of lithium-ion batteries (LIBs) in electric vehicles, the demand for lithium resources has surged. However, the natural abundance of lithium is only 0.0017 wt.%, which may be insufficient to meet the growing requirements for large-scale energy storage and electric vehicles.[1,2] To achieve sustainable energy development, it is imperative to identify low-cost and resource-abundant alternatives to complement lithium-ion batteries. In this context, potassium-ion batteries (KIBs) present a promising solution for large-scale energy storage, because potassium is more abundant in the Earth's crust (1.5 wt.%). The low standard hydrogen electrode potential of potassium in common carbonate electrolytes (K^+/K: −2.88 V, Na^+/Na: −2.56 V, Li^+/Li: −2.79 V), along with its low Lewis acidity and low desolvation energy, contributes to excellent electrolyte transport kinetics, which are critical to high-power applications.[3–6] However, the larger ionic radius of K^+ (1.38 Å) compared to Li^+ (0.76 Å) and Na^+ (1.02 Å) results in rapid capacity decay and poor rate capability due to significant volume changes in the host materials during K^+ insertion and extraction.[7,8] Therefore, the design of stable cathode materials for K-ion batteries is of paramount importance.

Currently, reported cathode materials for potassium-ion batteries (KIBs) include Prussian blue and its analogues,[9–11] layered transition metal oxides,[12–15] organic compounds,[16–18] and polyanionic compounds.[19–21] Among the various polyanionic compounds, fluorophosphate cathode materials like $KVPO_4F$, which possess a $KTiOPO_4$-type structure, have attracted significant interest on account of their high output voltage, substantial specific capacity, and stable framework featuring 3D ionic diffusion channels.[22–26] Komaba et al. were the first to evaluate $KVPO_4F$ as a cathode material for KIBs and demonstrated highly reversible potassium-ion extraction and insertion with a reversible discharge capacity of 92 mAh g^{-1} in the voltage window of 2.0–5.0 V.[27] Kim et al. have synthesized stoichiometric $KVPO_4F$ by a solid-state reaction and achieved a reversible capacity of 105 mAh g^{-1} with an average voltage of 4.3 V (vs K/K^+) and

J. Zhang, J. Xu, X. Li, Z. Duan, H. Zhou, X. Wang
Key Laboratory of Materials Physics
Ministry of Education
School of Physics
Zhengzhou University
Zhengzhou 450001, China
E-mail: junminxu@zzu.edu.cn; wxclhm@zzu.edu.cn

X. Zhang, J. Xu, D. Xiao, P. K. Chu
Department of Physics
Department of Materials Science and Engineering, and Department of Biomedical Engineering
University of Hong Kong
Tat Chee Avenue, Kowloon, Hong Kong 999077, China
E-mail: paul.chu@cityu.edu.hk

D. Xiao
International School of Microelectronics
Dongguan University of Technology
Dongguan 523808, China

The ORCID identification number(s) for the author(s) of this article can be found under https://doi.org/10.1002/smll.202505135

DOI: 10.1002/smll.202505135

an energy density of up to 450 Wh kg^{-1}.[28] However, $KVPO_4F$ faces some challenges, such as rapid capacity decay and poor rate capability because of its low electronic conductivity and unstable electrode/electrolyte interface at high voltages. To address these issues, integrating $KVPO_4F$ with carbon materials is an effective way to improve K-ion storage in $KVPO_4F$. For instance, Liu et al. have synthesized $KVPO_4F$ with a modified 3D amorphous carbon framework showing an average output voltage of 4.10 V and a high discharge capacity of 102.96 mAh g^{-1} at 20 mA g^{-1}.[29] Liao et al. have embedded $KVPO_4F$ primary particles in a carbon framework to attain a high capacity of 103.0 mAh g^{-1} at 20 mA g^{-1} and good cycling performance.[30] Xu et al. have incorporated reduced graphene oxide (rGO) into $KVPO_4F$ to produce hybrid graphene electrodes.[31] The rGO prevents $KVPO_4F$ particle aggregation and enhances ionic diffusion and electronic conductivity, resulting in a high discharge capacity of 103.2 mAh g^{-1} at 20 mA g^{-1}. Hence, the integration of rGO into $KVPO_4F$ enhances the electrochemical characteristics by preventing particle aggregation and improving electron conductivity. However, selecting the appropriate preparation method for the efficient formation of composites between $KVPO_4F$ and carbon materials remains a critical issue for potassium ion storage.

Direct ink writing (DIW) 3D printing has gained much attention as a promising technique for the development of high-performance electrodes.[32–36] This manufacturing technique constructs intricate 3D objects by layer-by-layer deposition of materials, composites, or solvent-based inks, guided by computer-aided design.[37] In contrast to conventional manufacturing methods, DIW 3D printing enables precise control over the electrode shape and mass loading through adjustments of the printing thickness and micropatterns. Furthermore, this technique addresses the challenges associated with designing electrodes that require specific porosity and high conductivity for optimal ion and electron transfer.[38,39] Recent research indicates that for the successful fabrication of high-performance graphene hybrid electrodes by DIW 3D printing,[40–42] it is important to have active materials well-dispersed in the graphene matrix in order to create a self-supporting electrode with enhanced electrical conductivity and efficient carrier transfer pathways. The integration of $KVPO_4F$ into a 3D reduced graphene oxide (rGO) matrix by advanced 3D printing techniques can improve the performance. The rGO matrix provides not only a 3D conductive network but also a buffer to mitigate mechanical stress during K-ion insertion and extraction, thereby enhancing cycling stability and facilitating rapid charge and discharge. Moreover, the rGO coating on $KVPO_4F$ acts as a physical barrier to prevent detrimental side reactions.

In this study, periodically porous $KVPO_4F$/reduced graphene oxide (KVPF/rGO) microgrid aerogel electrodes are fabricated by advanced 3D printing technology. The $KVPO_4F$ microspheres are synthesized by a solvothermal method and annealing, followed by hybridization with reduced graphene oxide using direct ink writing 3D printing. The freestanding KVPF/rGO aerogel electrodes deliver exceptional electrochemical performance for potassium-ion (K-ion) storage, such as a reversible discharge capacity of 99.0 mAh g^{-1} at a current density of 50 mA g^{-1}, capacity retention of 93.9% after 100 cycles, and rate performance of 72.6 mAh g^{-1} at 500 mA g^{-1}. Furthermore, the flexibility of the 3D-printed electrodes is validated by soft-pack batteries undergoing mechanical deformation, consequently boding well for wearable electronics.

2. Results and Discussion

The preparation process of the 3D-printed KVPF/rGO electrode is shown in **Figure 1**. The amorphous $KVPO_4F$ (KVPF) powder is synthesized by a solvothermal method at 180 °C for 6 h and then calcined under flowing argon at 700 °C for 5 h to produce highly crystalline KVPF (see Figure S1, Supporting Information). KVPF is mixed with graphene oxide (GO) and centrifuged to create the 3D printable ink. The 3D network pattern is printed by modified DIW ink-jet printing. Finally, the pattern is freeze-dried and annealed to produce the KVPF/rGO microgrid aerogel electrode. The DIW-based 3D printing technique offers advantages such as ease of operation and the ability to customize mass loading and complex shapes by varying the printing thickness and designed micropatterns.

The crystal structure of as-synthesized KVPF and 3D-printed KVPF/rGO is characterized by X-ray diffraction (XRD). **Figure 2a** shows that both KVPF and KVPF/rGO contain the orthorhombic $KTiOPO_4$ phase (JCPDS No.73-0130) with the space group of Pn21a. However, the XRD peaks originating from rGO are not observed from 3D-printed KVPF/rGO, possibly due to the low intensity of rGO, and that the peak of rGO at ≈26° may be screened by the main peaks of orthorhombic KVPF at 25.037°, 25.864°, and 26.433°.[43–45] Figure 2b shows that KVPF particles have a uniform spherical morphology, with each sphere being ~5 µm in diameter. The uniform spherical morphology is confirmed by TEM as depicted in Figure 2c. The TEM image of an individual KVPF microsphere and EDS elemental maps in Figure 2d confirm the presence of key elements K, V, P, O, and F. XPS is conducted to yield more elemental information. As shown in Figure 2e1, K, V, P, O, and F are present in KVPF. Figure 2e2 reveals peaks of potassium at 292.5 eV (K $2p_{3/2}$) and 295.3 eV (K $2p_{1/2}$), and Figure 2e3 shows peaks at 516.7 eV (V $2p_{3/2}$) and 524.2 eV (V $2p_{1/2}$) together with a small signal from V^{4+}, indicative of oxidation in air.[30] Figure 2e4 shows peaks at 132.8 eV (P═O) and 133.8 eV (P–F),[31] and Figure 2e5 shows the O–P peak at 530.8 eV and O–V peak at 532.5 eV.[46] Figure 2e6 shows the V–F peak at 684.7 eV. Collectively, XPS confirms the synthesis of KVPF microspheres. Consequently, the KVPF microspheres are used to prepare the KVPF/rGO microgrid aerogel electrode.

Figure 3a illustrates the capability to print complex-shaped KVPF/rGO aerogel electrodes, including intricate designs such as five-pointed stars and squares, on glass substrates. This design versatility is significant when the spatial configuration can influence the electrochemical properties. In addition, KVPF/rGO microgrid aerogel electrodes with dimensions of 2.0 cm × 2.0 cm are fabricated by DIW 3D printing, as shown in Figure 3b. The layer-by-layer printing process allows not only precise control of the electrode dimensions but also the adjustment of electrode thickness, as demonstrated in Figure 3c. Electrodes with 3, 6, 9, and 12 layers corresponding to thicknesses of 0.3, 0.6, 0.9, and 1.2 cm, respectively, are prepared, and the variable thickness highlights the potential to optimize the areal capacity of the electrodes, suggesting that thicker 3D-printed designs can enhance the energy storage capability. In this study, a KVPF/rGO aerogel electrode measuring 1.0 cm × 1.0 cm with a thickness of

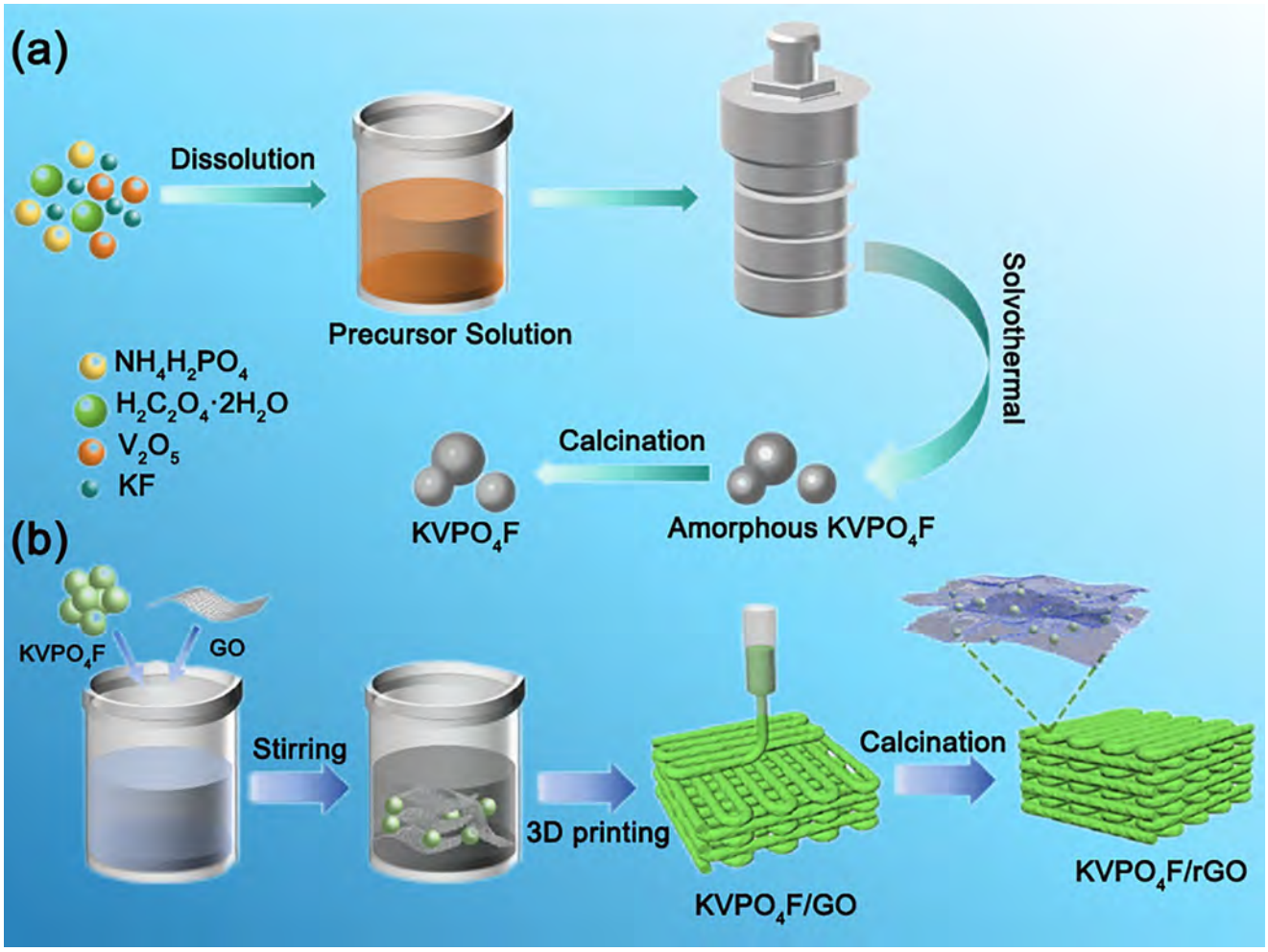

Figure 1. Schematic diagram of the fabrication process of a) $KVPO_4F$ and b) 3D-printed $KVPO_4F$/rGO microgrid aerogel.

3.0 mm is selected for further analysis and electrochemical assessment. Figure 3d showcases the intricate architecture of the 3D-printed KVPF/rGO microgrid aerogel, which features periodic submillimeter microchannels and a robust interconnected network of printed filaments. This design is particularly advantageous, as the microchannels facilitate ion transport and enhance electrolyte penetration, thereby improving the overall electrochemical properties. The filaments, composed of wrinkled graphene nanoflakes rich in micropores, have a large specific surface area, which is essential to maximizing the electrochemical interactions. The high-magnification scanning electron microscopy (SEM) images in Figure 3e,f1 disclose that the KVPF microspheres are uniformly encapsulated by rGO. Encapsulation is crucial to the establishment of a stable and conductive network in the composite electrode, since it enhances charge transport and reduces the resistance during electrochemical reactions. Energy-dispersive X-ray spectroscopy (EDS) mapping in Figure 3f2–f7 confirms the uniform distributions of potassium (K), vanadium (V), phosphorus (P), oxygen (O), and fluorine (F) in the composite, in addition to carbon (C) from rGO. The homogeneous distributions reflect a well-integrated composite, and these elements not only contribute to the structural integrity of the electrode but also play a pivotal role in the electrochemical activity and redox reactions that are fundamental to energy storage applications.

Cyclic voltammetry (CV) is employed to study the potassium storage behavior of the KVPF and 3D-printed KVPF/rGO electrodes. **Figure** 4a presents the curves of the three initial CV cycles of KVPF and 3D-printed KVPF/rGO in the voltage range between 2.0 and 5.0 V at a scanning rate of 0.1 mV s^{-1}. The CV curves of both electrodes exhibit remarkable similarity and good overlap throughout the tested cycles, with each displaying multiple pairs of redox peaks. This observation indicates that both electrode types undergo analogous multi-step potassium intercalation and deintercalation processes, confirming their functional similarity in terms of potassium-ion dynamics during the tested cycles. The CV curve of the 3D-printed KVPF/rGO electrode exhibits larger integral areas under the redox peaks at higher voltages, suggesting enhanced electrochemical activity in this voltage range compared to the KVPF electrode. The larger area under the redox peaks reflects a higher potassium ion storage capacity and faster kinetics of the 3D-printed composite. The higher conductivity of KVPF in the rGO matrix, facilitated by the 3D printing process, plays a crucial role in activating additional electrochemical processes at elevated potentials. Figure 4b shows

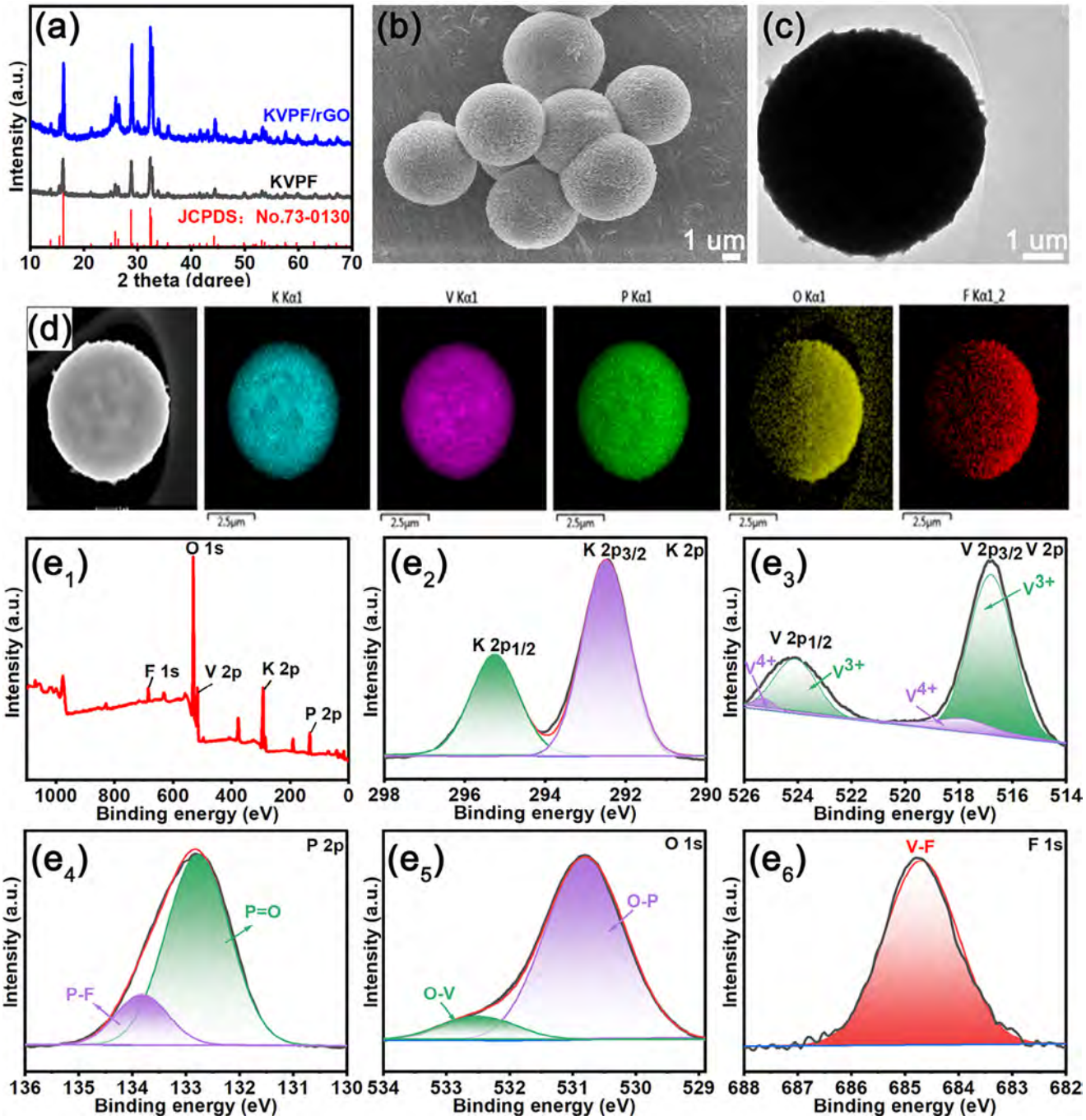

Figure 2. a) XRD patterns of KVPF and KVPF/rGO; b) SEM and c) TEM images of KVPF microspheres; d) TEM image of a single KVPF microsphere with the corresponding EDS elemental maps; e_1) XPS survey spectrum of KVPF and high-resolution XPS spectra of KVPF: e_2) K 2*p*, e_3) V 2*p*, e_4) P 2*p*, e_5) O 1s, and e_6) F 1s.

the three initial charge–discharge profiles of the KVPF and 3D-printed KVPF/rGO electrodes at a current density of 50 mA g^{-1} in the voltage window between 2.0 and 5.0 V. Both electrodes exhibit similar charge–discharge profiles for the cycles, indicating that they have a comparable electrochemical behavior. The KVPF electrode shows a broad average charge–discharge potential plateau ≈4.37 V for charging and 3.92 V for discharging. This plateau is primarily attributed to the redox reactions between V^{3+} and V^{4+} and the associated extraction and insertion of K^+ in the $K_{1-x}VPO_4F$ framework. In contrast, the 3D-printed KVPF/rGO electrode shows plateaus at slightly lower potentials of 4.36 V during charging and 3.95 V during discharging. This observation suggests reduced polarization in the 3D-printed composite compared to the KVPF electrode. It can be linked to the enhanced ionic and electronic conductivity stemming from the integration of KVPF into the rGO matrix. The first specific discharge

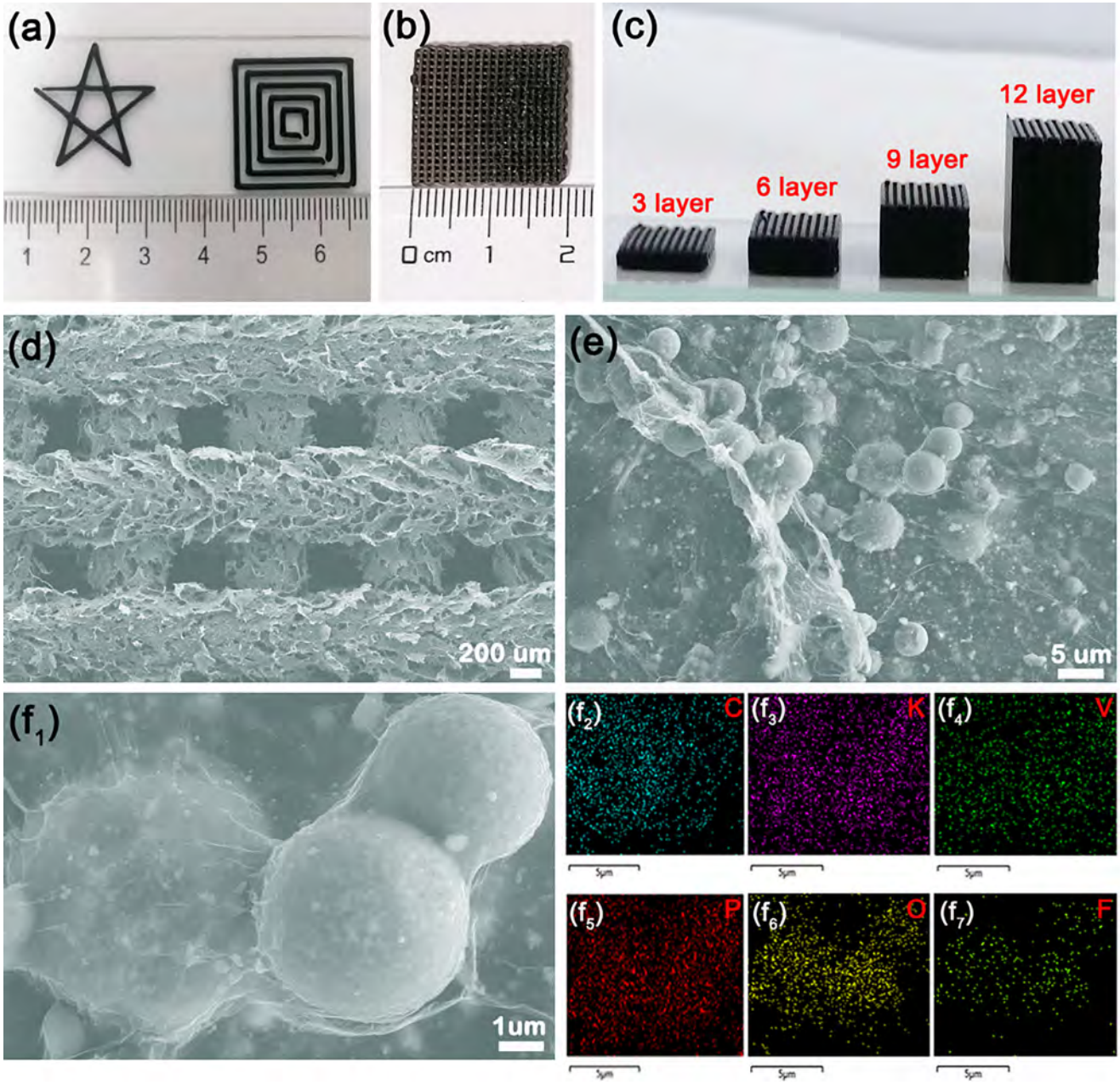

Figure 3. a) KVPF/rGO aerogel patterns printed by the 3D printing; b) Photographs of a 3D printed KVPF/rGO microgrid aerogel measuring 2.0 cm×2.0 cm; c) Images of the 3D-printed printed KVPF/rGO microgrid aerogel with different layers (3, 6, 9, and 12 layers); (d,e) SEM images of the KVPF/rGO microgrid aerogel at different magnifications; f_1–f_7) High-resolution SEM images of the KVPF/rGO aerogel and EDS maps of C, K, V, P, V, O, and F.

capacities of the KVPF and 3D-printed KVPF/rGO electrodes are 70.3 and 99.0 mAh g^{-1}, respectively, showing a significant improvement in energy storage of the 3D-printed hybrid structure. Moreover, the discharge capacity of the 3D-printed KVPF/rGO electrode remains stable in the next two cycles, with values of 96.9 and 96.2 mAh g^{-1} for the 2nd and 3rd cycles, respectively, implying good electrochemical stability during the initial three cycles.

To further investigate the electrochemical processes during the charge–discharge cycles, ex situ X-ray photoelectron spectroscopy (XPS) is conducted on the 3D-printed KVPF/rGO electrodes. As shown in Figure 4c, the high-resolution V 2*p* spectra reveal two distinct valence states: V^{3+} (peaks at ≈516.9 and 524.0 eV) and V^{4+} (peaks at ≈517.8 and 525.3 eV). During the initial charging process, a progressive increase in the peak intensity associated with V^{4+} ions is observed, while the intensity of the V^{3+} ions decreases gradually. After reaching a charge voltage of 5.0 V, the ratio of V^{4+} to V^{3+}, derived from the integral areas of the peaks, is determined to be ≈1:0.39, resulting in a final average vanadium valence state of +3.72. During the

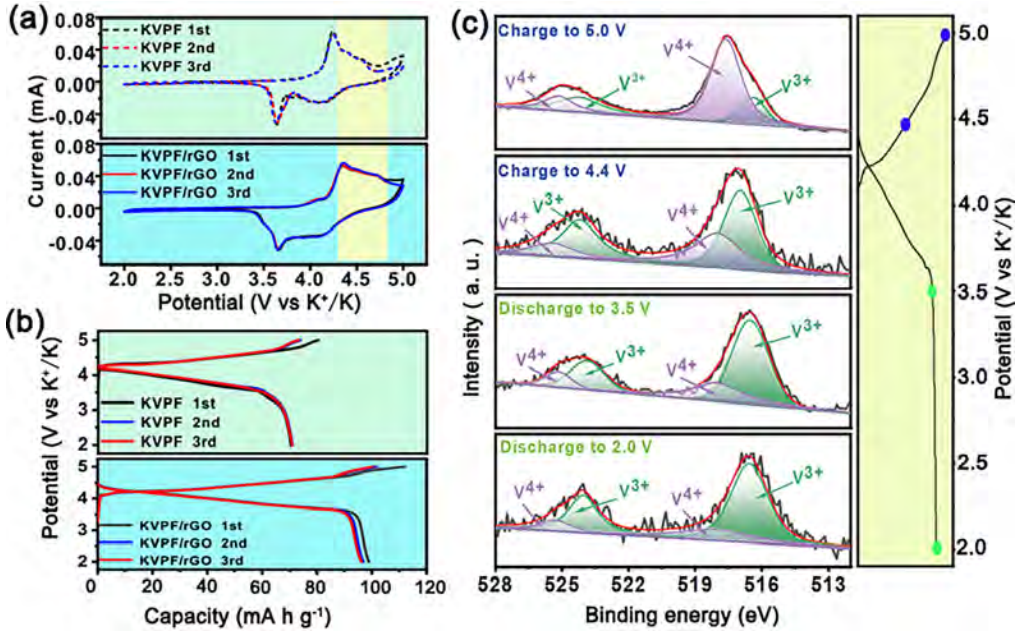

Figure 4. a) CV profiles of the KVPF and 3D-printed KVPF/rGO electrodes at a scanning rate of 0.1 mV s^{-1}. b) First three charging/discharging profiles of KVPF and 3D-printed KVPF/rGO at 50 mA g^{-1}; c) Ex situ high-resolution XPS V 2*p* spectra of the 3D-printed KVPF/rGO cathodes in different stages.

subsequent discharging process, the intensity of the V^{3+} peak increases while that of the V^{4+} peak diminishes. At a discharge voltage of 2.0 V, the ratio of V^{4+} to V^{3+} is calculated to be 1:3.81, yielding a final mean vanadium valence state of ≈+3.20. This variation reflects the reversible de-intercalation and intercalation of 0.52 mol of K^+ ions in the 3D-printed KVPF/rGO material and also demonstrates the capability to undergo reversible electrochemical transformations efficiently.

Figure 5a compares the cycling stability of the KVPF and 3D-printed KVPF/rGO electrodes at a current density of 50 mA g^{-1}. The 3D-printed KVPF/rGO electrode has good cycling properties, such as a capacity retention of 93.9% after 100 cycles. In contrast, the KVPF electrode not only shows a low initial discharge capacity of 70.3 mAh g^{-1} but also suffers from rapid capacity decay by retaining only 83.9% of its discharge capacity after 100 cycles. To explore the underlying causes of capacity degradation in the KVPF electrode, SEM images of both KVPF and 3D-printed

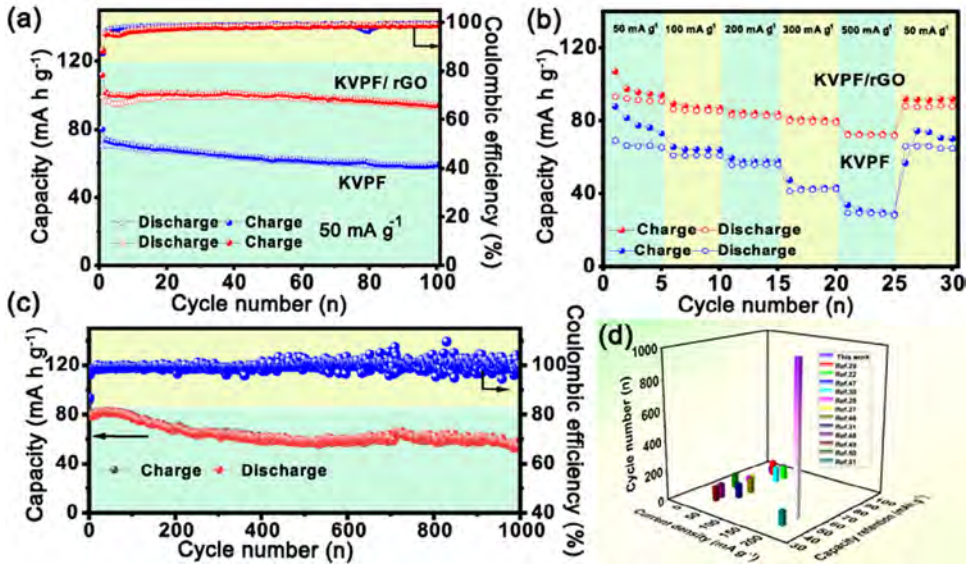

Figure 5. a) Cycling characteristics of the KVPF and 3D-printed KVPF/rGO electrodes at 50 mA g^{-1}; b) Rates of KVPF and 3D-printed KVPF/rGO at different discharge current rates from 50 to 500 mA g^{-1}; c) Long-term cycling properties of KVPF/rGO at 200 mA g^{-1}; d) Comparison of potassium-ion storage performance between the 3D-printed KVPF/rGO aerogel and similar electrodes reported in the literature.

KVPF/rGO electrodes were captured before and after 100 cycles. As shown in Figure S4 (Supporting Information), the KVPF electrode displayed prominent cracking after repeated cycling. The ongoing development of these cracks may lead to a progressive loss of electrical contact within the KVPF material, ultimately diminishing its capacity performance. In contrast, the 3D-printed KVPF/rGO electrode largely preserved its original morphology and structural integrity following cycling. This is likely attributed to the KVPF being tightly encapsulated within the conductive rGO framework. Furthermore, the 3D conductive network created by rGO effectively maintains electrical contact with the active KVPF material, thereby contributing to good cycling stability and enhanced capacity output. To further assess the rapid charging and discharging capabilities of both electrodes, the rate performance is evaluated, as shown in Figure 5b. The KVPF electrode shows average discharge capacities of 65.9, 61.1, 55.8, and 41.6 mAh g^{-1} at current densities of 50, 100, 200, and 300 mA g^{-1}, respectively. When the current density is increased to 500 mA g^{-1}, the KVPF electrode can only deliver an average discharge capacity of 30.0 mAh g^{-1}, indicating its limited rate capability. In contrast, the 3D-printed KVPF/rGO electrode exhibits higher average discharge capacities of 91.2, 85.8, 83.1, and 79.4 mAh g^{-1} at the same current densities. Remarkably, even at a current density of 500 mA g^{-1}, it still provides an average discharge capacity of 72.6 mAh g^{-1}. Furthermore, when the current density is reverted back to 50 mA g^{-1}, the 3D-printed KVPF/rGO electrode retains a discharge capacity of 87.7 mAh g^{-1}, which is very close to its initial capacity, demonstrating good recovery of rate capability. These results clearly indicate that the 3D-printed KVPF/rGO electrode has superior rate capability compared to the KVPF electrode. The long-term stability of the 3D-printed KVPF/rGO electrode is evaluated at a higher current density of 200 mA g^{-1}. As shown in Figure 5c, the electrode shows good cycling characteristics, including a discharge capacity of 53.8 mAh g^{-1} after 1000 cycles and a capacity retention of 68.0%. Figure 5d illustrates the electrochemical potassium-ion storage properties of various vanadium-based polyanion cathode materials. A comparative analysis of the electrochemical properties highlights the advantages of the 3D-printed KVPF/rGO aerogel electrode in comparison to other vanadium-based polyanion cathodes.[46–51] The underlying mechanisms contributing to the enhanced electrochemical performance of the 3D-printed KVPF/rGO electrode were investigated using in situ electrochemical impedance spectroscopy (EIS). **Figure 6** presents the in situ EIS results for both the 3D-printed KVPF/rGO electrode and the KVPF electrode at specified charging and discharging states. Following data fitting and calculations (see Figure 6a1,a2), the charge transfer impedance (Rct) of the 3D-printed KVPF/rGO electrode exhibits a trend of initially decrease followed by an increase throughout the entire charging and discharging cycle. This behavior indicates stable interfacial characteristics and high reversibility during the tested charging and discharging processes. Upon discharging to 2.5 V, the Rct value for the 3D-printed KVPF/rGO electrode is 2597.85 Ω, which is significantly lower than that of the KVPF electrode at 19385.14 Ω (see Figure 6b1,b2). This observation suggests that the reduced graphene oxide conductive network enhances electronic conductivity and improves charge storage kinetics. Multi-scan rate cyclic voltammetry (CV) was employed to further investigate the reaction kinetics of the 3D-printed KVPF/rGO electrode (see **Figure 7**a). As the scan rate increases, notable shifts in the CV peaks are observed. These peak shifts can be analyzed using Equation (1):[52,53]

$$i = av^b \tag{1}$$

where v represents the scan rate and i denotes the peak current. A parameter b = 0.5, indicates that diffusion predominantly controls charge storage, while b = 1 signifies capacitive-controlled charge storage. The fitted b values of peak I and peak II are found to be 0.84 and 0.79, respectively (see Figure 7b), suggesting that the kinetics of K^+ storage in the 3D-printed KVPF/rGO electrode is influenced by both diffusion and capacitive mechanisms. To quantify the contributions of diffusion-controlled and capacitive-controlled processes, we performed calculations according to Equation (2):[52,53]

$$i = k_1 v + k_2 v^{1/2} \tag{2}$$

For example, the CV profile indicates that the capacitive contribution at a scan rate of 1.0 mV s^{-1} accounts for ~84% of the total measured current, demonstrating a surface-controlled, capacitive-dominant process (see Figure 7c). As illustrated in Figure 7d, the capacitive contribution (ranging from 55% to 84%) of the total current increases gradually with increasing scanning rates (from 0.2 to 1.0 mV s^{-1}), surpassing that of the KVPF electrode (see Figure S5, Supporting Information). This trend indicates that enhanced electrochemical kinetics in the 3D-printed KVPF/rGO aerogel electrode is primarily governed by capacitance at elevated current densities. Building on our analysis of reaction kinetics, we have elucidated the intrinsic mechanisms contributing to the enhanced performance of the 3D-printed KVPF/rGO electrode, as depicted in Figure 7e. This figure demonstrates how the hierarchical porous framework facilitates electrochemical potassium-ion storage. The 3D electrode, characterized by an open lattice structure and an abundance of micropores, promotes electrolyte penetration, ensuring sufficient contact between the electrolyte and electrode while accelerating K^+ diffusion at a microscopic level. Additionally, the 3D conductive network established by the rGO backbone enables rapid electron transport along interconnected filaments, while the vertically oriented micro-channels create expanded pathways for efficient ion and electron transport, even in thicker electrodes. Furthermore, the 3D rGO network imparts the necessary mechanical strength and durability to the KVPF microspheres. Consequently, the 3D-printed KVPF/rGO aerogel electrode exhibits good electrochemical potassium-ion storage properties.

To assess the practical potential of 3D-printed KVPF/rGO, flexible soft-pack batteries with 3D-printed KVPF/rGO as the positive electrode and molten metal potassium deposited on 3D-printed rGO as the negative electrode are fabricated, as shown in **Figure 8**a. Figure 8b presents the relationship between the number of printing layers and the KVPF mass loading for electrodes with different thicknesses. The linear increase in actual thickness with the number of printing layers shown in Figure 8c reveals a consistent and reproducible process, which can be scaled up readily for mass production. The charging and discharging curves in Figure 8d for the 2, 4, 6, and 8-layer 3D-printed KVPF/rGO electrodes show that the electrochemical

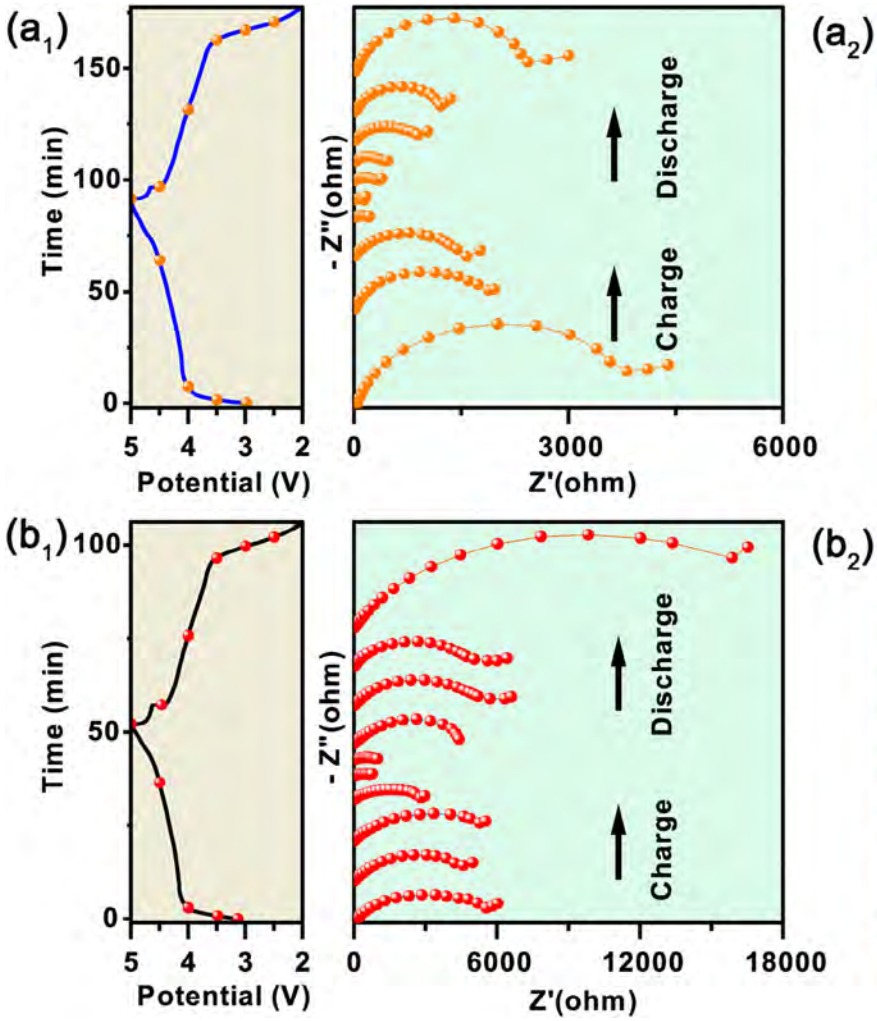

(a2)

Static potential	Rs (Ω)	Rct (Ω)
Discharge to 2.5 V	17.57	2597.85
Discharge to 3.0 V	15.36	1292.41
Discharge to 3.5 V	13.63	887.27
Discharge to 4.0 V	14.03	378.06
Discharge to 4.5 V	13.75	290.53
Charge to 5.0 V	12.16	63.17
Charge to 4.5 V	9.77	180.62
Charge to 4.0 V	13.12	1437.48
Charge to 3.5 V	13.90	1949.34
Charge to 3.0 V	16.74	4061.12

(b2)

Static potential	Rs (Ω)	Rct (Ω)
Discharge to 2.5 V	12.44	19385.14
Discharge to 3.0 V	13.85	5158.35
Discharge to 3.5 V	11.81	5422.04
Discharge to 4.0 V	10.72	5022.93
Discharge to 4.5 V	4.19	923.51
Charge to 5.0 V	15.91	619.06
Charge to 4.5 V	5.09	2731.48
Charge to 4.0 V	9.21	6128.57
Charge to 3.5 V	9.58	5481.16
Charge to 3.0 V	12.17	5975.32

Figure 6. a_1) In situ electrochemical impedance spectra (EIS) of the 3D-printed KVPF/rGO electrode at different charge/discharge stages; a_2) The fitted values of resistances Rs and Rct derived from the EIS for 3D-printed KVPF/rGO electrode. b_1) In situ electrochemical impedance spectra of the KVPF electrode at different charge/discharge stages; b_2) The fitted values of resistances Rs and Rct derived from the EIS for the KVPF electrode.

characteristics are consistent for different layer counts, suggesting that increasing the electrode thickness does not compromise electrochemical potassium-ion storage. The thicker electrodes with more printing layers have better areal capacities. As shown in Figure 8e, the first discharge areal capacity goes up from 0.154 to 0.287, 0.424, and 0.563 mAh cm^{-2} as the number of printed layers increases from 2 to 4, 6, and 8, respectively. Hence, optimizing the layer count can improve the energy density. The increase in areal capacity is particularly significant, as it impacts the energy storage capability. Furthermore, the 3D-printed KVPF/rGO electrodes are stable for 50 cycles, as shown by capacity retention rates of 102.1%, 100.2%, 94.8%, and 95.4% for the respective layer counts. The excellent stability stems from the structural robustness and electrochemical resilience of the printed electrodes. To further explore the potential of 3D-printed KVPF/rGO as flexible battery electrodes, 2 layers of KVPF/rGO are printed on a porous aluminum mesh substrate and paired with molten metal potassium on 3D-printed rGO as the negative electrode to produce flexible batteries. The electrochemical potassium storage properties of the flexible soft-pack battery are evaluated under various bending conditions: no bending, 45°, 90°, and 180°. As shown in Figure 8f, it maintains a high and stable specific capacity in addition to good Coulombic efficiency under different bending conditions. Figure 8g1–g5 illustrate the capability of the flexible soft-pack battery to continuously power a small fan under different bending conditions. Moreover, as shown in Figure 8h1–h5, these LEDs can be powered by a single KIB battery under various bending conditions for several hours. Our findings provide new information on how 3D printing can be used to develop high-performance potassium-ion batteries (KIBs) for flexible and portable applications. The ability to withstand mechanical stress is especially essential for wearable electronics.

3. Conclusion

A 3D-printed KVPF/rGO microgrid aerogel electrode is designed and fabricated for potassium-ion batteries (KIBs). The incorporation of the KVPF into the reduced graphene oxide (rGO) matrix by

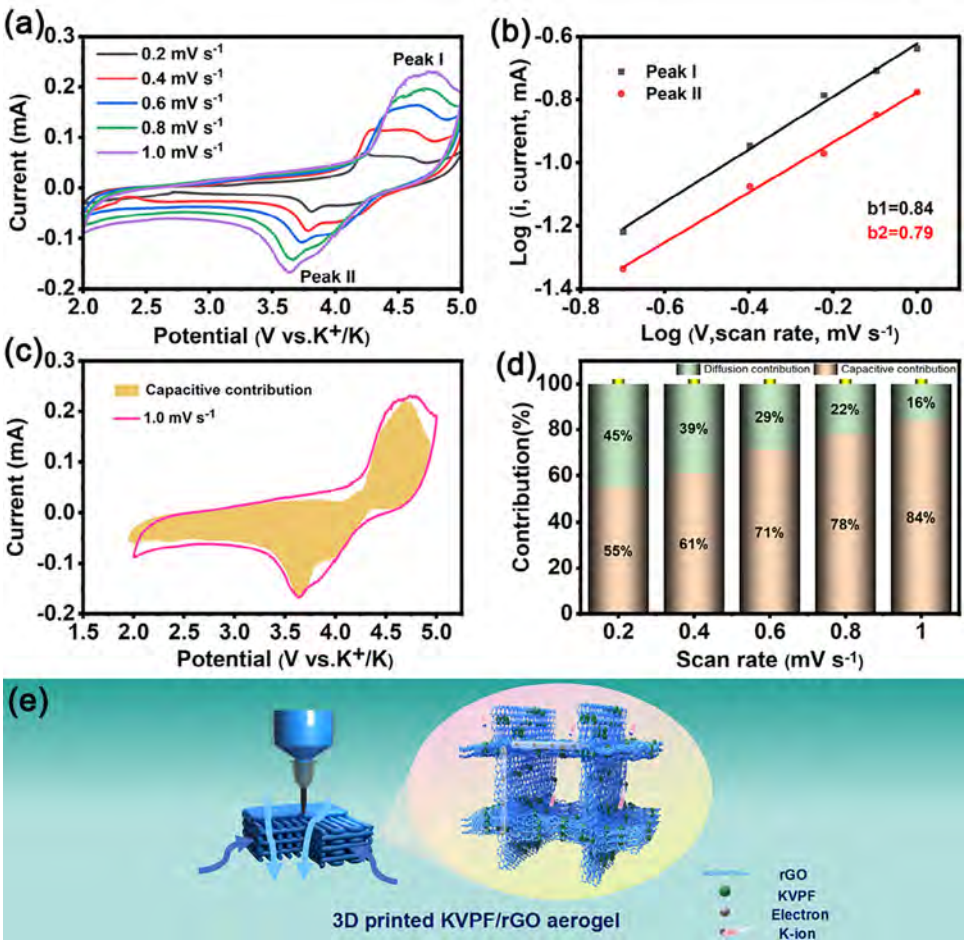

Figure 7. a) CV curves of the 3D-printed KVPF/rGO electrode at different scanning rates; b) Log(i) and log(v) plots of the 3D-printed KVPF/rGO electrode at peak currents and corresponding fitted b values; c) Capacitive contributions of the 3D-printed KVPF/rGO electrode at 1.0 mV s^{-1}; d) Contribution ratio of the capacitive-controlled current (or capacity) at different scan rates; e) Schematic illustration of the 3D-printed KVPF/rGO aerogel electrode with the hierarchical porous framework for enhanced electrochemical potassium-ion storage.

direct ink writing (DIW) enhanced the structure and conductivity, leading to more efficient ion transport. The KVPF/rGO electrode shows a reversible discharge capacity of 99.0 mAh g^{-1} at 50 mA g^{-1} and capacity retention of 93.9% after 100 cycles. Moreover, it shows a discharge capacity of 72.6 mAh g^{-1} at a high current density of 500 mA g^{-1}. The results underscore the effectiveness of the rGO matrix in improving charge transfer and reducing polarization. The flexibility of the 3D-printed electrodes and potential for wearable electronics are validated by fabricating soft-pack batteries and operating under different mechanical deformations. Overall, the potential of 3D printing to enhance potassium-ion battery performance and flexibility is demonstrated, and our results pave the way for future studies on advanced materials and manufacturing techniques for energy storage applications.

4. Experimental Section

Synthesis of $KVPO_4F$ (KVPF) Microspheres: To synthesize KVPF microspheres, a precursor solution was prepared by dissolving 4 mmol ammonium dihydrogen phosphate ($NH_4H_2PO_4$, ≥99%, Aladdin), 6 mmol potassium fluoride (KF, ≥99%, Aladdin), 2 mmol vanadium pentoxide (V_2O_5, 99%, Meryer), and 0.4 mmol oxalic acid dihydrate ($H_2C_2O_4{\cdot}2H_2O$, ≥99%, Aladdin) in a mixture of 10 mL of deionized water and 40 mL of ethylene glycol (≥99%, Meryer). The solution was stirred vigorously at room temperature for 2 h until a uniform yellow solution was obtained. Subsequently, the homogeneous solution (40 mL) was transferred to a 50 mL reactor with a polytetrafluoroethylene (PTFE) liner. The reactor was sealed and heated in an oven to 180 °C for 6 h. After the solvothermal reaction, the reactor was allowed to cool naturally to room temperature. The precipitate was collected and washed several times with deionized water and anhydrous ethanol. The product was then dried in an oven at 60 °C. Finally, the dried powder was placed in a high-temperature tube furnace under an argon atmosphere and calcined at 700 °C for 5 h to obtain the pure-phase KVPF with high crystallinity.

Preparation of the KVPF/GO Ink and 3D-Printed KVPF/rGO Microgrid Aerogel: To prepare the KVPF/graphene oxide (GO) ink, a mixture of 100 mg of KVPF powder and 30 mL of a GO aqueous solution (5 mg mL^{-1}) was homogenized and then centrifuged at 20 000 rpm for 30 min. This process yielded a 3D printing ink with the active component constituting 40% of the total mass. After thorough grinding, the paste was loaded into a syringe connected to a direct ink writing (DIW) 3D printer with a 150 µm inner diameter micronozzle. The microgrid pattern was printed through this nozzle, while the printing pressure was maintained between 0.15 and 0.25 MPa and the syringe was moved at a speed of 5 mm s^{-1}. After printing, the electrode was freeze-dried at −40 °C for 48 h to remove excess

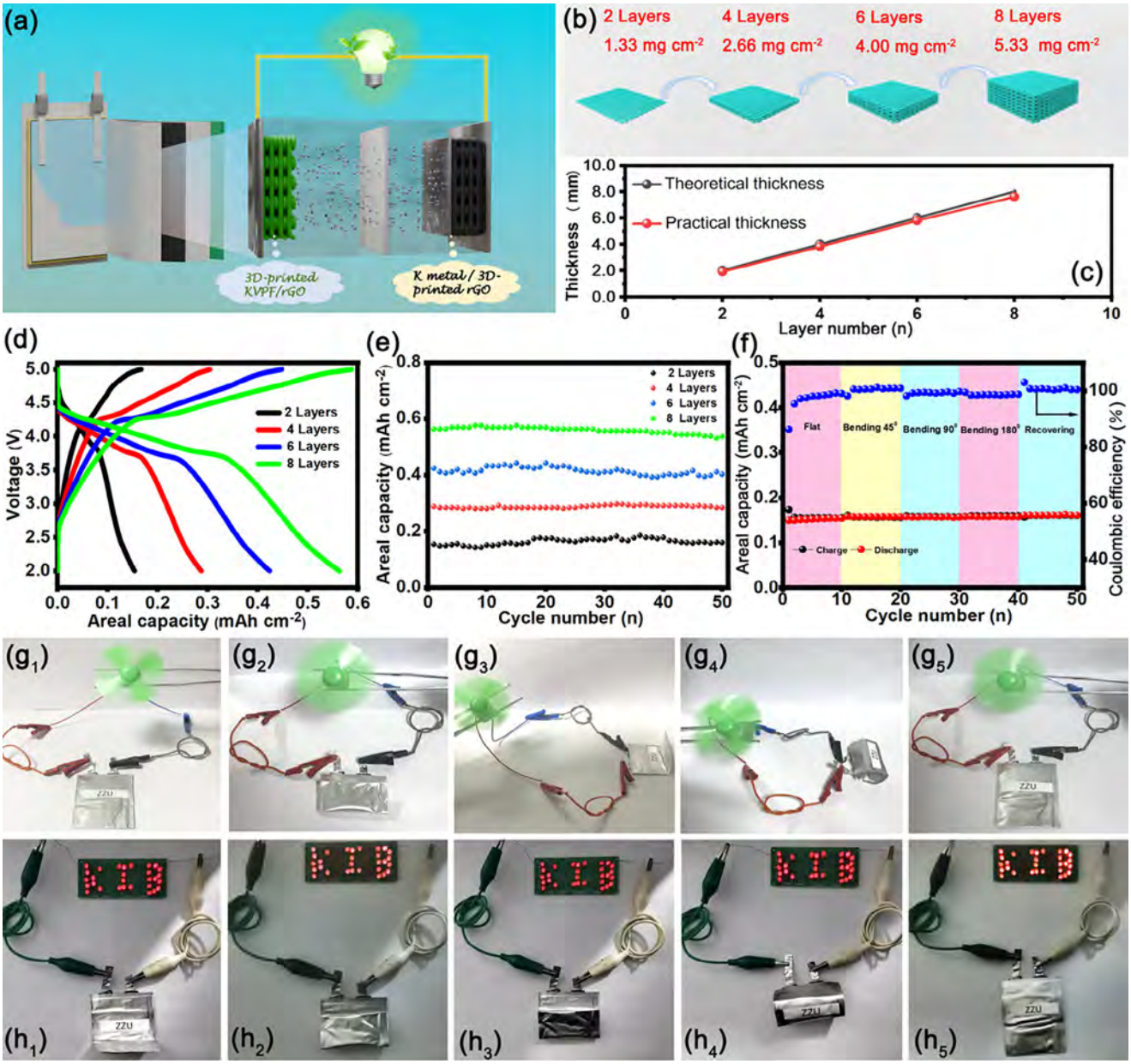

Figure 8. a) Schematic illustration of the soft-type KIB battery comprising the 3D-printed KVPF/rGO as the cathode; b) Schematic illustration of 3D-printed KVPF/rGO electrodes with different layers and masses; c) Practical and theoretical thicknesses of the 3D-printed electrodes as a function of the printing layer number; d) Charging–discharging curves of the 3D-printed KVPF/rGO electrodes with different layers; e) Cyling characteristics of the 3D-printed KVPF/rGO electrodes with different layers at a current density of 0.05 mA cm^{-2}; f) Cycling stability of the soft-type KIB battery under different mechanical deformations; g_1–g_4) Photos of the soft-type KIB battery powering a fan under various conditions; h_1–h_4) Photos of the soft-type KIB battery powering an LED bulb array under various conditions.

water while preserving the porous structure. The electrode was then annealed to convert GO to reduced graphene oxide (rGO) for enhanced electrical conductivity. The temperature was increased gradually to 600 °C at a rate of 2 °C min^{-1} in an argon atmosphere, and the temperature was held for 2 h. After cooling to room temperature, the KVPF/rGO self-supported electrode was obtained.

Materials Characterization: Scanning electron microscopy (SEM, JEOL JSM-6700F) was employed to observe the surface structure and overall morphology of the electrodes. Transmission electron microscopy (TEM, JEOL JEM-2100) and high-resolution transmission electron microscopy (HRTEM) were utilized to examine the internal structure on the nanoscale. Energy-dispersive X-ray spectroscopy (EDS) was performed using the EDS module in the TEM to determine the elemental composition of the samples. The crystal structures of KVPF and KVPF/rGO were determined by X-ray diffraction (XRD) using Cu Kα radiation. The composition and chemical states of the materials were analyzed by X-ray photoelectron spectroscopy (XPS) on the ESCALAB 250Xi system (Thermo Fisher, USA).

Electrochemical Measurements: The 3D-printed KVPF/rGO microgrid aerogel, 1.0 cm × 1.0 cm × 3.0 mm thick, was the working electrode in the electrochemical tests. For comparison, traditional $KVPO_4F$

electrodes were prepared using a mixture with a mass ratio of 7:2:1 of $KVPO_4F$:Super P:polyvinylidene fluoride (PVDF) dissolved in N-methyl-2-pyrrolidone (NMP, ≥99%, Aladdin). The slurry was applied to an aluminum foil and vacuum-dried overnight at 120 °C to ensure complete solvent removal before electrode assembly. The coin-type (CR2032) cells were assembled in an argon-filled glovebox, in which the oxygen and moisture levels were less than 0.5 ppm to prevent any contamination. Potassium was used as the anode, and a Whatman glass microfiber filter (GF/D) served as the separator. The electrolyte was 0.5 M KPF_6 dissolved in a mixture of fluoroethylene carbonate (FEC) and propylene carbonate (PC) with a volume ratio of 1:1, which provided the suitable ionic conductivity and stability for the electrochemical cell operation.

To prepare the flexible pouch-type battery, a KVPF/rGO microgrid with dimensions of 5.0 cm × 5.0 cm was printed onto a porous aluminum foil as the cathode. The 3D-printed rGO aerogel on the porous aluminum foil was placed in molten potassium metal, and after cooling to room temperature, it served as the anode. The assembly of the flexible battery involved placing the KVPF/rGO microgrid/Al foil and the rGO anode/Al foil loaded with potassium metal in proximity. It was then encapsulated with a plastic film to provide the structural integrity and protection against environmental factors. This design allows for enhanced flexibility and lightweight characteristics, making it suitable for various applications where traditional rigid battery formats may not be ideal.

Supporting Information

Supporting Information is available from the Wiley Online Library or from the author.

Acknowledgements

This work was supported by the National Natural Science Foundation of China (Grant No. 51802288), the Foundation of basic research for young teachers of Zhengzhou University (JC23549005), and City University of Hong Kong Donation Research Grants (DON-RMG 9229021 and 9220061).

Conflict of Interest

The authors declare no conflict of interest.

Data Availability Statement

The data that support the findings of this study are available in the supplementary material of this article.

Keywords

3D-printing, flexible potassium ion batteries, high-performance cathode, $KVPO_4F$/rGO aerogel

Received: April 27, 2025
Revised: July 5, 2025
Published online: September 4, 2025

[1] K. Kubota, M. Dahbi, T. Hosaka, S. Kumakura, S. Komaba, *Chem. Rec.* **2018**, *18*, 459.
[2] K. Sada, J. Darga, A. Manthiram, *Adv. Energy Mater.* **2023**, *13*, 2302321.
[3] W. C. Zhang, J. Lu, Z. P. Guo, *Mater. Today* **2021**, *50*, 400.
[4] S. Dhir, S. Wheeler, I. Capone, M. Pasta, *Chem* **2020**, *6*, 2442.
[5] Y. F. Xu, Y. C. Du, H. Chen, J. Chen, T. J. Ding, D. M. Sun, D. H. Kim, Z. Q. Lin, X. S. Zhou, *Chem. Soc. Rev.* **2024**, *53*, 7202.
[6] S. Dai, C. Yang, Y. Wang, Y. Jiang, L. Zeng, *Adv. Sci* **2025**, *12*, 2500513.
[7] X. Min, J. Xiao, M. H. Fang, W. Wang, Y. J. Zhao, Y. G. Liu, A. M. Abdelkader, K. Xi, R. V. Kumar, Z. H. Huang, *Energ. Environ. Sci.* **2021**, *14*, 2186.
[8] R. Rajagopalan, Y. G. Tang, X. B. Ji, C. K. Jia, H. Y. Wang, *Adv. Funct. Mater.* **2020**, *30*, 1909486.
[9] L. Li, Z. Hu, Y. Lu, C. C. Wang, Q. Zhang, S. Zhao, J. Peng, K. Zhang, S. L. Chou, J. Chen, *Angew. Chem., Int. Ed.* **2021**, *60*, 13050.
[10] L. Q. Deng, J. L. Qu, X. G. Niu, J. Z. Liu, J. Zhang, Y. R. Hong, M. Y. Feng, J. W. Wang, M. Hu, L. Zeng, Q. F. Zhang, L. Guo, Y. J. Zhu, *Nat. Commun.* **2021**, *12*, 2167.
[11] X. Y. Li, X. L. Zhang, J. M. Xu, Z. X. Duan, Y. Xu, X. S. Zhang, L. L. Zhang, Y. Wang, P. K. Chu, *Adv. Sci.* **2024**, *11*, 2305467.
[12] Z. T. Xiao, J. S. Meng, F. J. Xia, J. S. Wu, F. Liu, X. Zhang, L. H. Xu, X. M. Lin, L. Q. Mai, *Energ. Environ. Sci.* **2020**, *13*, 3129.
[13] Y. H. Zhu, Q. Zhang, X. Yang, E. Y. Zhao, T. Sun, X. B. Zhang, S. Wang, X. Q. Yu, J. M. Yan, Q. Jiang, *Chem* **2019**, *5*, 168.
[14] X. Li, C. F. Zhuang, J. M. Xu, L. Li, T. T. Xu, S. G. Dai, X. C. Wang, X. J. Li, Y. Wang, *Nanoscale* **2021**, *13*, 8199.
[15] M. G. T. Nathan, H. Yu, G. T. Kim, J. H. Kim, J. S. Cho, J. Kim, J. K. Kim, *Adv. Sci.* **2022**, *9*, 2105882.
[16] W. S. Zhang, W. W. Huang, Q. C. Zhang, *Chem.-Eur. J.* **2021**, *27*, 6131.
[17] Y. Hu, W. Tang, Q. H. Yu, X. X. Wang, W. Q. Liu, J. H. Hu, C. Fan, *Adv. Funct. Mater.* **2020**, *30*, 2000675.
[18] D. D. Yu, H. Wang, W. Zhang, H. F. Dong, Q. N. Zhu, J. Yang, S. M. Huang, *Energy Storage Mater.* **2021**, *43*, 172.
[19] K. Y. Zhang, Z. Y. Gu, E. H. Ang, J. Z. Guo, X. T. Wang, Y. L. Wang, X. L. Wu, *Mater. Today* **2022**, *54*, 189.
[20] B. F. Ji, W. J. Yao, Y. P. Zheng, P. Kidkhunthod, X. L. Zhou, S. Tunmee, S. Sattayaporn, H. M. Cheng, H. Y. He, Y. B. Tang, *Nat. Commun.* **2020**, *11*, 1225.
[21] S. S. Fedotov, N. D. Luchinin, D. A. Aksyonov, A. V. Morozov, S. V. Ryazantsev, M. Gaboardi, J. R. Plaisier, K. J. Stevenson, A. M. Abakumov, E. V. Antipov, *Nat. Commun.* **2020**, *11*, 1484.
[22] J. Y. Liao, X. X. Zhang, Q. H. Zhang, Q. Hu, Y. F. Li, Y. C. Du, J. Z. Xu, L. Gu, X. S. Zhou, *Nano Lett.* **2022**, *22*, 4933.
[23] X. D. He, L. M. Zhang, C. H. Jiang, C. H. Chen, *Chem. Eng. J.* **2022**, *433*, 134634.
[24] Y. Zhu, B. Ou, C. Gao, Y. Gao, B. Zhang, F. Kang, D. Zhai, *ACS Energy Lett.* **2024**, *9*, 3212.
[25] C. Xie, X. W. Liu, J. Han, L. Lv, X. Zhou, C. H. Han, Y. You, *Small* **2022**, *18*, 2204348.
[26] X. R. Yang, D. N. Yan, T. M. Chou, J. C. Kim, *J. Mater. Chem. A* **2023**, *11*, 14304.
[27] K. Chihara, A. Katogi, K. Kubota, S. Komaba, *Chem. Commun.* **2017**, *53*, 5208.
[28] H. Kim, D. H. Seo, M. Bianchini, R. J. Clément, H. Kim, J. C. Kim, Y. S. Tian, T. Shi, W. S. Yoon, G. Ceder, *Adv. Energy Mater.* **2018**, *8*, 1801591.
[29] Z. M. Liu, J. Wang, B. A. Lu, *Sci. Bull.* **2020**, *65*, 1242.
[30] J. Y. Liao, Q. Hu, X. D. He, J. X. Mu, J. R. Wang, C. H. Chen, *J. Power Sources* **2020**, *451*, 227739.
[31] J. Z. Xu, J. Y. Liao, Y. F. Xu, J. B. Li, C. N. Zhu, J. Lin, X. S. Zhou, *J. Energy Chem.* **2022**, *68*, 284.
[32] S. G. Dai, Z. L. Lin, H. Hu, Y. Wang, L. H. Zeng, *Appl. Phys. Rev.* **2024**, *11*, 041319.
[33] W. L. Bai, H. Wang, D. H. Min, J. Z. Miao, B. M. Li, T. T. Xu, D. Z. Kong, X. J. Li, X. Yu, Y. Wang, H. S. Park, *Adv. Sci.* **2024**, *11*, 2404419.

[34] D. H. Pan, H. Y. Yang, Y. Y. Liu, H. Wang, T. T. Xu, D. Z. Kong, J. J. Yao, Y. M. Shi, X. J. Li, H. Y. Yang, Y. Wang, *Nanoscale* **2023**, *15*, 17493.
[35] M. P. Browne, E. Redondo, M. Pumera, *Chem. Rev.* **2020**, *120*, 2783.
[36] Q. Xu, N. Chu, Y. Wang, H. Wang, T. Xu, X. Li, S. Huang, X. Li, Y. Luo, H. Y. Yang, D. Kong, *Adv. Sci.* **2025**, *12*, 2401660.
[37] T. Han, Z. Y. He, W. Q. Kuang, J. Zhou, Y. Y. Li, *Nano Energy* **2024**, *128*, 109953.
[38] M. P. Browne, F. Novotny, Z. Sofer, M. Pumera, *ACS Appl. Mater. Interfaces* **2018**, *10*, 40294.
[39] T. K. Chu, S. Park, K. Fu, *Carbon Energy* **2021**, *3*, 424.
[40] B. B. Guo, G. J. Liang, S. X. Yu, Y. Wang, C. Y. Zhi, J. M. Bai, *Energy Storage Mater.* **2021**, *39*, 146.
[41] Z. X. Duan, X. L. Zhang, J. M. Xu, N. N. Chu, J. W. Zhang, M. F. Ji, X. C. Wang, D. Z. Kong, Y. Wang, P. K. Chu, *Small* **2024**, *20*, 2405430.
[42] M. Liu, D. Kong, N. Chu, G. Zhi, H. Wang, T. Xu, X. Wang, X. Li, Z. Zhang, H. Y. Yang, Y. Wang, *Adv. Sci.* **2025**, *12*, 2417638.
[43] C. F. Hua, Y. Y. Shang, X. Y. Li, X. Y. Hu, Y. Wang, X. C. Wang, Y. J. Zhang, X. J. Li, H. L. Duan, A. Y. Cao, *Nanoscale* **2016**, *8*, 10659.
[44] B. Zhang, C. F. Yu, Z. J. Li, *Nanoscale Res. Lett.* **2020**, *15*, 184.
[45] K. J. Chen, X. Li, J. H. Zang, Z. F. Zhang, Y. Wang, Q. Lou, Y. C. Bai, J. T. Fu, C. F. Zhuang, Y. Zhang, L. L. Zhang, S. G. Dai, C. X. Shan, *Nanoscale* **2021**, *13*, 12370.
[46] J. Z. Xu, L. P. Duan, J. Y. Liao, H. W. Tang, J. Lin, X. S. Zhou, *Green Energy Environ.* **2023**, *8*, 1469.
[47] Y. W. Byeon, M. J. Gong, Z. Cai, Y. Sun, N. J. Szymanski, J. Bai, D. H. Seo, H. Kim, *Energy Storage Mater.* **2023**, *57*, 81.
[48] W. B. Park, S. C. Han, C. Park, S. U. Hong, U. Han, S. P. Singh, Y. H. Jung, D. Ahn, K. S. Sohn, M. Pyo, *Adv. Energy Mater.* **2018**, *8*, 1703099.
[49] X. D. He, J. Y. Liao, T. Chen, L. M. Zhang, X. Ding, J. R. Wang, S. Wang, Z. Y. Wen, C. H. Chen, *J. Alloy. Compd.* **2021**, *884*, 161126.
[50] J. F. Li, Y. S. Zheng, K. S. Hui, K. X. Wang, C. Y. Zha, D. A. Dinh, J. G. Tu, Z. P. Shao, K. N. Hui, *Energy Storage Mater.* **2023**, *61*, 102852.
[51] H. X. Kuai, J. F. Lu, X. Y. Lv, J. Su, Y. F. Long, Y. X. Wen, *Ionics* **2022**, *28*, 3817.
[52] X. Li, J. Fu, M. Sun, S. Cheng, K. Chen, X. Yang, Q. Lou, T. Xu, Y. Shang, J. Xu, Q. Chen, C. Shan, *Nanoscale* **2019**, *11*, 13343.
[53] Y. Wang, Y. V. Lim, S. Huang, M. Ding, D. Kong, Y. Pei, T. Xu, Y. Shi, X. Li, H. Y. Yang, *Nanoscale* **2020**, *12*, 4341.

3D-Printed $KVPO_4F$/rGO aerogel electrodes as high-performance 5V-class cathode for advanced potassium-ion battery

Jinwei Zhang, Xiaolin Zhang, Junmin Xu, Xinyue Li, Dezhi Xiao, Zhixia Duan, Han Zhou, Xinchang Wang*, and Paul K. Chu**

* Corresponding author.

J. Zhang, X. Li, J. Xu, Z. Duan, H. Zhou, X. Wang

Key Laboratory of Materials Physics, Ministry of Education, School of Physics, Zhengzhou University, Zhengzhou 450001, China

Email: junminxu@zzu.edu.cn (J. Xu); wxclhm@zzu.edu.cn (X. Wang)

X.Zhang, J. Xu, D.Xiao, P. K. Chu

Department of Physics, Department of Materials Science and Engineering, and Department of Biomedical Engineering, City University of Hong Kong, Tat Chee Avenue, Kowloon, Hong Kong, China

Email:paul.chu@cityu.edu.hk (P. K. Chu);

D.Xiao

International School of Microelectronics, Dongguan University of Technology, Dongguan, 523808, China

Supporting Figures

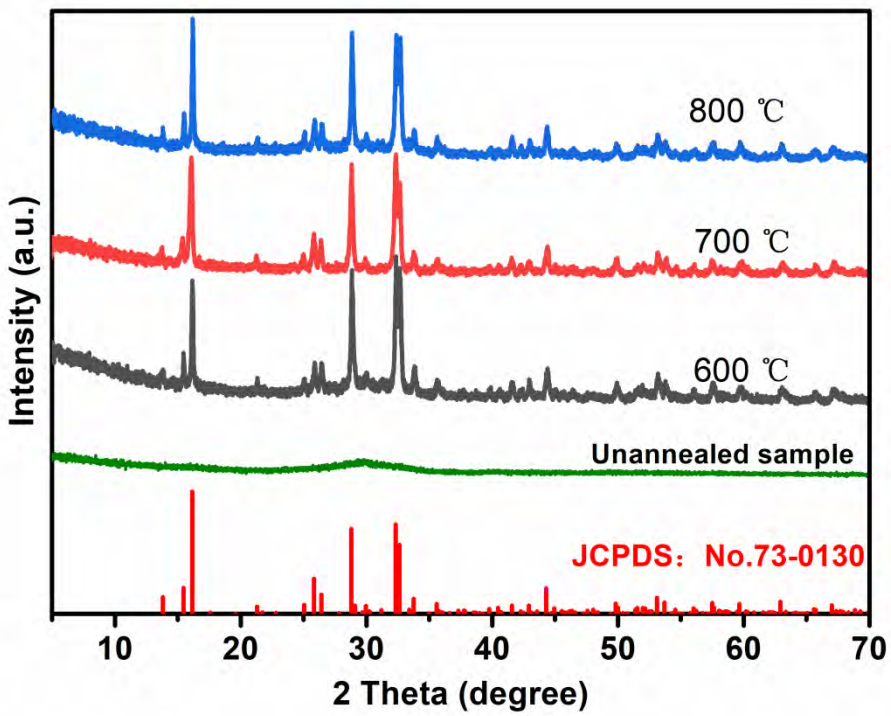

Figure S1. XRD patterns of unannealed $KVPO_4F$ and $KVPO_4F$ subjected to annealing at different temperatures.

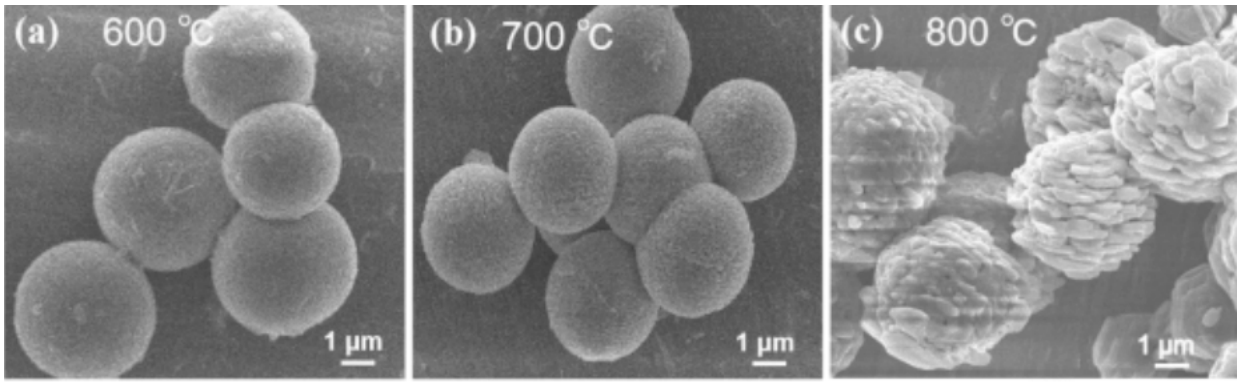

Figure S2. The SEM images of $KVPO_4F$ synthesized at different annealing temperatures: (a) 600 °C; (b) 700 °C; (c) 800 °C.

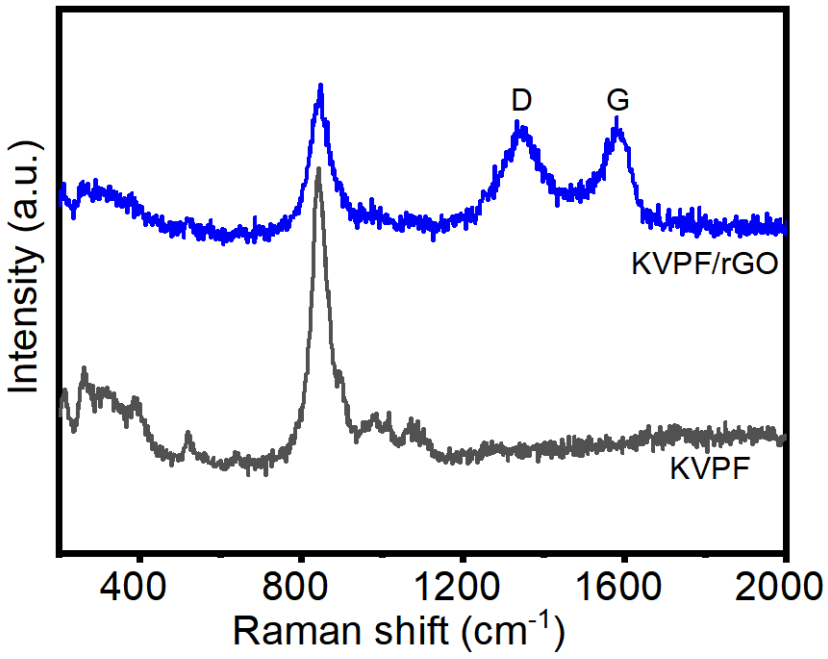

Figure S3. Raman spectra of KVPF and KVPF/rGO.

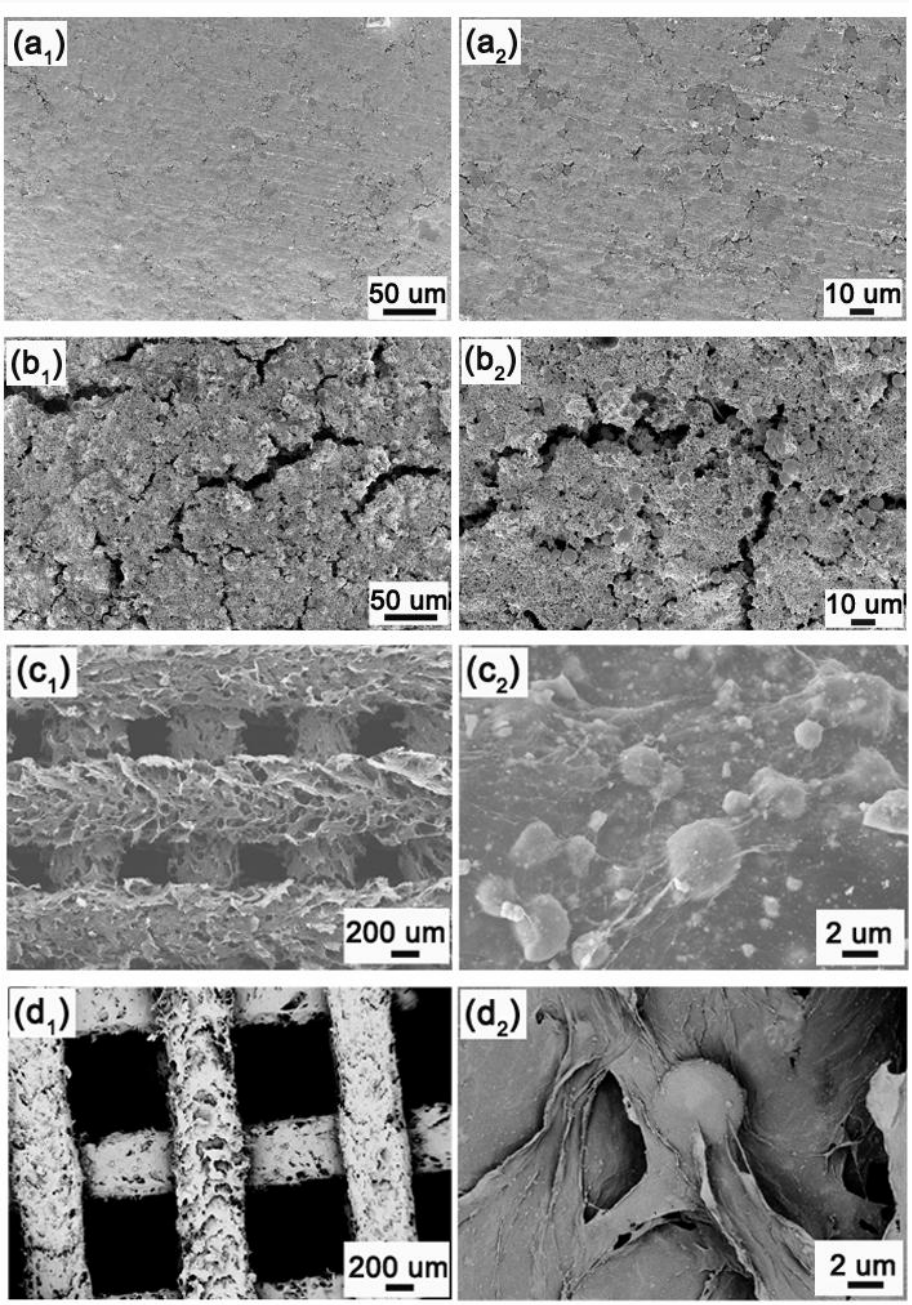

Figure S4. SEM images of the KVPF electrode before (a_1, a_2) and after (b_1, b_2) 100 cycles at a current density of 50 mA g^{-1}; SEM images of the 3D-printed KVPF/rGO electrode before (c_1, c_2) and after (d_1, d_2) 100 cycles at a current density of 50 mA g^{-1}.

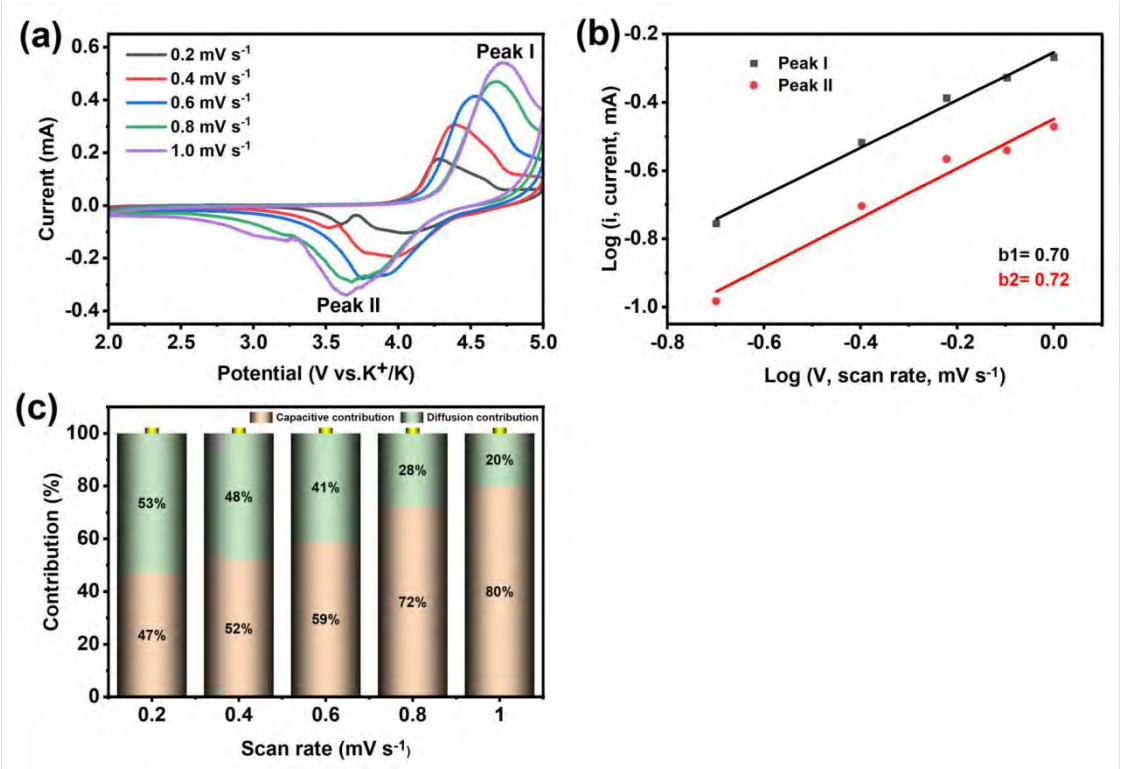

Figure S5. (a) CV curves of the KVPF electrode at different scanning rates; (b) Log(i) and log(v) plots of the KVPF electrode at peak currents and corresponding fitted b values; (c) Contribution ratio of the capacitive-controlled current (or capacity) at different scan rates.